CONFERENCE PRE-PRINT

SIMULATION STUDY OF THE EFFECT OF IMPURITYS ON THE NONLINEAR DYNAMIC PROCESS OF EDGE-LOCALIZED-MODES

T.H. HUANG

School of Nuclear Science and Technology, University of Science and Technology of China Hefei, P.R. China

Email: huangth@mail.ustc.edu.cn

T.Y. LIU

School of Nuclear Science and Technology, University of Science and Technology of China Hefei, P.R. China

S.F. MAO

School of Nuclear Science and Technology, University of Science and Technology of China Hefei, P.R. China

M.Y. YE

School of Nuclear Science and Technology, University of Science and Technology of China Hefei, P.R. China

Abstract

To explore the underlying mechanism of complicated response of ELM behavior to the impurities, a systemic simulation study is carried out using BOUT++ six-field two-fluid model extended with impurity equations based on the EAST experiment with impurity seeding. Linear simulation shows impurity has overall stabilizing effect to the pedestal, which is mainly through extra vorticity induced by impurity and can be characterized by impurity mass density ratio. While linear growth rate shows a monotonic reduction with increasing impurity density, the reduction of simulated ELM size has a "threshold" for the impurity density in nonlinear simulation. Further analysis explains this complicated phenomenon by the combined effects of peeling-ballooning mode and drift tearing mode. The impurity effect on the ELM behaviour is concluded in the parameter space.

1. INTRODUCTION

It is crucial to avoid large edge-localized modes (ELMs) to achieve high confinement steady plasma operation state. While the radiative impurities are necessary for achieving divertor detachment especially for the future tokamak [1], it is also found to have essential effects on ELM control [2]. Therefore, the mechanism how impurities affect the dynamic of ELMs is of great concern. Simulation studies based on "indirect" effects of impurities, such as radiative cooling, profile regulation and fuel dilution, have been considered in the linear instability analysis [3-5], which is insufficient to explain the complicated ELM behaviors observed in experiments [6, 7].

In this work, a systematical simulation study of the dynamical effect of impurities on pedestal stability and ELM evolution is carried out. The simulations are performed using BOUT++ six-field two-fluid module [8], where the impurity model developed by Li et al. [9] (for studying the impurity dynamics in ELM-free QH-mode) is integrated. The simulations are implemented with self-consistent n = 0 electric field and parallel current evolution according to Seto et al.'s work [10, 11]. In addition, electron inertia is also considered for self-consistent current dissipation in fast magnetic reconnection.

2. IMPURITY EFFECT WITHIN THE SIMULATION MODEL

Compared to the original model [8], the dynamic effect of impurities are primarily reflected in the vorticity expression:

$$\varpi = \frac{m_{i}}{B} \left(\nabla_{\perp} \cdot \left(n_{\mu 0} \nabla_{\perp} \phi \right) + \frac{1}{Z_{i} e} \nabla_{\perp}^{2} \left(P_{i} + \frac{A_{imp}}{A_{i}} \frac{Z_{i}}{Z_{imp}} P_{imp} \right) \right). \tag{1}$$

Here, A and Z are the atomic mass and charge number. Subscript i/imp represents main plasma ion (deuterium) and impurity ion, respectively. The effective density is $n_{\mu 0} = n_{i0} + \left(A_{imp}/A_i\right) n_{imp0}$. In typical tokamak fusion plasmas, the main ion species are deuterium and tritium, which have substantially lower ion mass number (~2 and 3) compared to impurity ions, such as neon (~20) and argon (~40). Therefore, the introduction of impurities leads to a significant increase in the effective density, which also reflects to the plasma inertia. It is reasonable to infer that the increased plasma inertia probably leads to the smaller perturbation amplitude under the same free energy drive, thereby effectively suppressing the instability.

Another important mechanism is due to the net vorticity introduced by impurity. In tokamak pedestal plasmas, impurities mentioned above typically exhibit a high degree of ionization. For instance, under typical EAST parameters, neon ions predominantly exist in the 8+ charge state within the pedestal region. While main ion has nearly no net poloidal drift flow with neoclassical radial electric field $E_{r0} \sim \nabla_r P_{i0}/en_{i0}$, impurity has significant net poloidal drift flow, thus ultimately providing a equilibrium vorticity. In simulation, with equilibrium electric field chosen as $E_{r0} = \nabla_r P_{i0}/en_{i0}$, the equilibrium vorticity introduced by impurity is

$$\boldsymbol{\varpi}_{0} = \frac{\boldsymbol{m}_{i}}{B} \left(\nabla_{\perp} \cdot \left(\frac{A_{\text{imp}}}{A_{i}} \boldsymbol{n}_{\text{imp0}} \nabla_{\perp} \boldsymbol{\phi} \right) + \frac{1}{Z_{i} e} \nabla_{\perp}^{2} \left(\frac{A_{\text{imp}}}{A_{i}} \frac{Z_{i}}{Z_{\text{imp}}} \boldsymbol{P}_{\text{imp0}} \right) \right). \tag{2}$$

To investigate the complicate response of ELM to the impurities, the simulation study in this work is based on the EAST equilibrium shot #69033. Equilibrium profiles at t = 3.95s profile with type-III small ELM before impurity seeding and t = 4.495s profile with large ELM after impurity seeding are chosen.

Only one impurity species (Ne^{8+}) is considered, and initial impurity density is simply calculated by $N_{\text{imp0, base}} = (N_{e0} - N_{i0})/8$ for preliminary study, where electron density is from microwave reflectometer and ion density is estimated with constant Z_{eff} assumption (see ref [6]).

3. LINEAR SIMULATION RESULTS

Linear growth rate of 3.95s profile, and that of 4.495s profile with different impurity effects are shown in Fig. 1. It can be observed that without any impurity effect, the growth rate of 4.495s is significantly larger than 3.95s for entire toroidal modes. It is because of the increase of density gradient, which is already discussed in Ref. [6]. When considering the increase of inertia due to impurities, the growth rate of high toroidal mode number n becomes smaller, while that of moderate n becomes even larger, contrast with the general expectation of stabilizing effect of inertia. When considering initial vorticity introduced by impurity, the growth rate is significantly reduced for all n modes, even lower than growth rate of 3.95s.

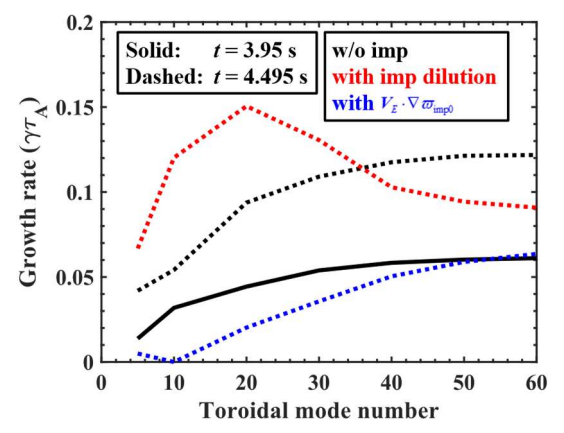


Fig. 1 Linear growth rate vs. toroidal mode number.

Through localized eigenmode analysis, the ballooning mode growth rate γ_b with impurity is:

$$\gamma_b^2 \propto \frac{1}{n_i \alpha |1 - C|} \left(1 - \frac{R_{\text{imp}}}{|1 - C|} \right).$$
(3)

Here, α is a positive constant related with equilibrium electric potential, $R_{\rm imp} = A_{\rm imp} n_{\rm imp} / \left(A_{\rm imp} n_{\rm imp} + A_{\rm i} n_{\rm i}\right) = 1 - n_i / n_\mu$ is impurity mass density ratio and C is a constant related to the ion pressure gradient.

As a validation, the square of simulated growth rate of n = 10 mode with different R_{imp} are explored and shown in Fig. 2. It can be observed that, the effect of impurity on the linear growth rate can be characterized by R_{imp} . Different types of impurity have similar effect with same R_{imp} and the trend of the square of growth rate with R_{imp} shows good agreement with analysis above.

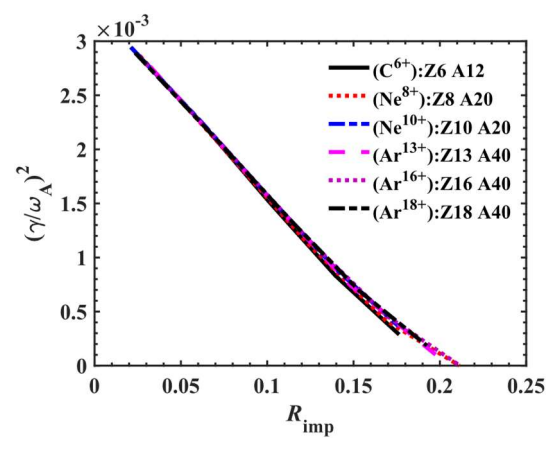


Fig. 2 Square of the linear growth rate of n = 10 mode vs. R_{imp} .

4. NONLINEAR SIMULATION RESULTS

Both simulation and analysis indicate that the impurity dynamics has stabilizing effect on linear instability. However, further research with nonlinear simulation shows more complicated responses of ELM behavior with impurities.

The simulated ELM size evolutions with impurity density scanning are shown in Fig. 3. It can be observed that, the nonlinear response of ELM to impurity has distinct difference to the linear case. Unlike the monotonic reduction of instability with impurity density increase observed in linear simulations, a threshold is found in the nonlinear response of ELM size to impurity density. When impurity density is below this threshold, although the evolution is affected, the final energy loss remains nearly unaffected. Conversely, when impurity density exceeds the threshold, the ELM size decreases with increasing impurity density.

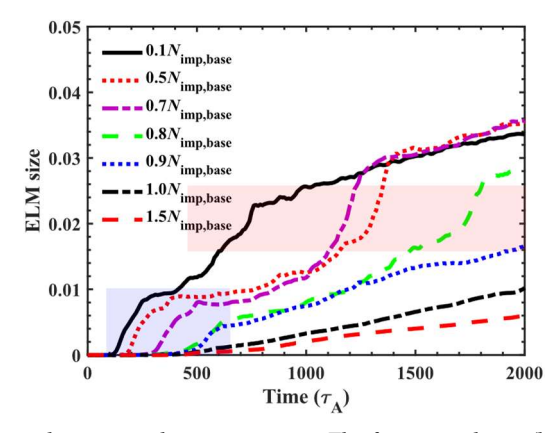


Fig. 3 Time evolution of ELM size with impurity density scanning. The first stage burst (burst A) is marked by blue shading, and the second stage burst (burst B) is marked by red shading.

Furthermore, two stage of burst can be observed, as shown in cases " $0.1 \sim 0.8 N_{\text{imp, base}}$ " in Fig. 3. While the impurity density is lower than threshold, although the increase of impurity density reduces the amplitude of first burst, however, when the second burst occurs, the ELM sizes become similar. Only when the impurity density is increased until the second burst is completely suppressed, the total ELM size can be reduced and continuously reduce with the increase of impurity density.

As Fig. 3 cases " $0.8 \sim 1.0 \ N_{imp, base}$ " show, these two stages of burst are suppressed in turn, which indicates that they can exist independently, implying there is probably different mechanism for each burst. According to the evolution of pressure perturbations, the first stage occurs at the end of linear growth of peeling-ballooning mode, which is a typical burst induced by growth of peeling-ballooning instability in general nonlinear simulations. The second burst occurs in nonlinear stage, after the saturation of perturbation, which implies the burst is probably triggered by nonlinear mechanism. Since two bursts can exist individually, in order to avoid confusion, the burst connected with P-B mode growing is marked as "burst A", and the other one is marked as "burst B".

The triggering of "burst B" is found to be closely connected to the reduction of toroidal axisymmetric (n = 0) radial electric field shear. The time evolution of the amplitude of n = 0 radial electric field shear with different radial wavenumbers are shown in Fig. 4. Here, for simplicity, the different wavenumber component is calculated by Fourier transform in radial direction, and the field shear is characterized by

$$\left| \frac{\partial \left\langle E \right\rangle_{k_r}}{\partial r} \right| \sim \left| k_r \left\langle E \right\rangle_{k_r} \right|,\tag{4}$$

where the angle bracket refers to the toroidal average. It is observed that, the shear amplitude with radial wavenumber $k_r \sim 400~{\rm m}^{-1}$ is significantly reduced to the minimal value before "burst B" occurs (see the red dotted line at the moment marked by red dashed line in Fig. 4). As discussed in linear analysis, impurities suppress ELM by enhancing shear stabilization effect, which is related to the shear of n=0 radial electric field. With the n=0 radial electric field shear reduces, the stabilizing effect of impurity reduces accordingly, leading to a burst of ELM in nonlinear phase. And due to the reduction of impurity stabilizing effect, finally simulated ELM size shows almost unaffected by the impurity density unless "burst B" is completely suppressed (see Fig. 3), which exhibits a "threshold" phenomenon.

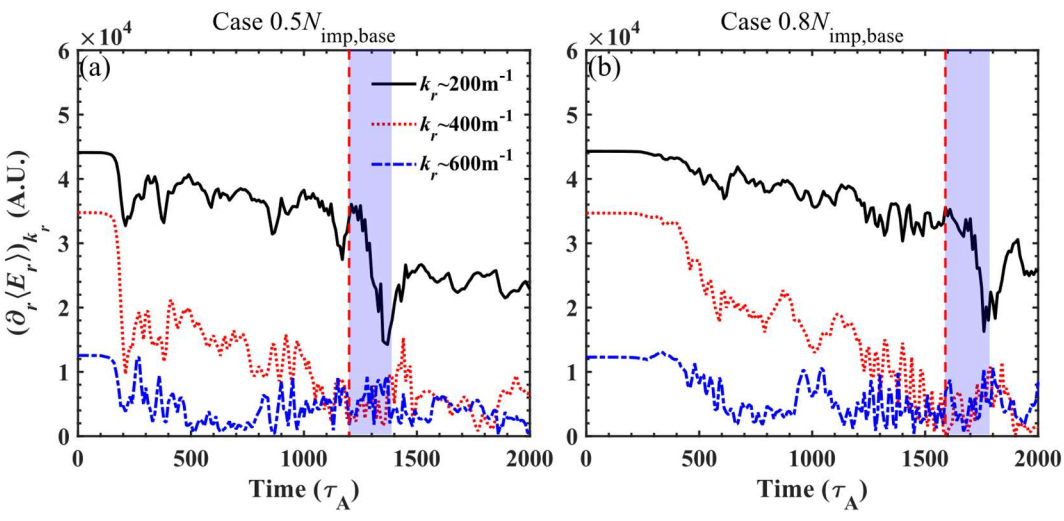


Fig. 4 Time evolution of the amplitude of n = 0 radial electric field shear with different radial wavenumbers in (a) case 0.5 Nimp, base and (b) case 0.8Nimp, base. The time range of "burst B" is marked by blue shading, and the beginning of burst is highlighted by red dashed line.

Further analysis shows the reduction of electric field shear is due to the increase of magnetic flutter, which is driven by drift tearing mode.

Time evolution of the variation of radial electric field shear and contribution from magnetic flutter in case "0.8 $N_{\text{imp, base}}$ " is shown in Fig. 5. These quantities are calculated by:

$$T_{\text{magnetic flutter}} = \frac{\partial}{\partial t} \left(\left| \frac{\partial}{\partial r} \langle E_r \rangle_{k_r} \right|^2 \right)_{\text{magnetic flutter}} \sim -\frac{2n_{\mu 0} B_0}{m_i} \text{Real} \left[\left(B_0^2 \nabla_{\parallel 1} \frac{j_{\parallel 1}}{B_0} \right)_{k_r} \times \left(\frac{\partial}{\partial r} \langle E_r \rangle_{k_r} \right)^* \right]$$
 (5)

Here, subscript "magnetic flutter" means the variation of the radial electric field shear caused by magnetic flutter effect, superscript "*" means taking conjugate and Real means taking real part. It can be observed that the reduction of n = 0 electric field before "burst B" ($t \le 1600\tau_A$) is almost contributed by the magnetic flutter effect. It implies the reduction of radial electric field is dominated by the magnetic flutter.

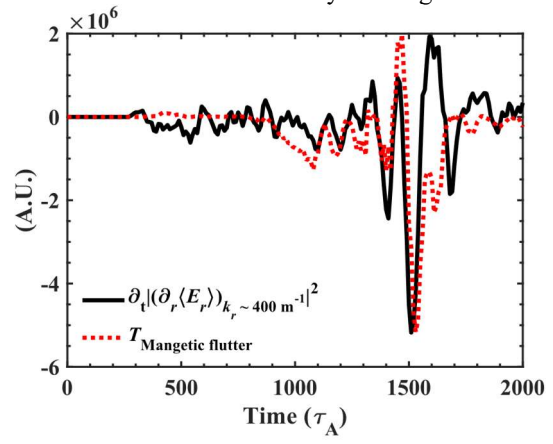


Fig. 5 The time evolution of the variation of radial electric field shear amplitude and the contribution from magnetic flutter.

The generation mechanism of magnetic flutter is considered to be the drift-tearing-mode (DTM), which is mainly driven by the electron temperature gradient and the growth rate has the form $\gamma_{\rm DTM} \propto \omega_{\rm *e}^2/v_{\rm e} \sim T_{\rm e}^{7/2}N_{\rm e}^{-1}Z_{\rm eff}^{-1}\left(T_{\rm e}'/T_{\rm e}\right)$ [12]. As a validation, a series of linear simulations were conducted by scanning electron temperature (ion temperature is accordingly adjusted to remain total pressure unchanged), with both peeling and ballooning drives removed. The scatter plot of linear growth rate vs. electron temperature on a log-log scale is shown in Fig. 6. Here, the electron temperature is chosen at the location of the steepest pressure gradient on the outer midplane. Since the scanning of electron temperature is by multiplying a constant ratio, so that $T_{\rm e}'/T_{\rm e}$ is constant, the simulated growth rate and electron temperature satisfies $\ln(\gamma_{\rm DTM}) \sim 7/2\ln(T_{\rm e})$. The linear fit to the simulation data points demonstrates good agreement with the theoretical prediction.

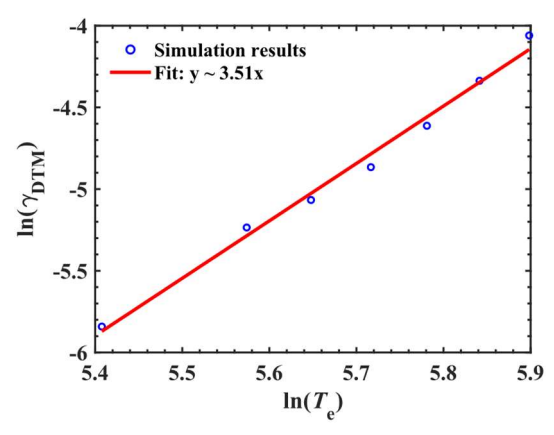


Fig. 6 Growth rate of magnetic perturbation energy vs. equilibrium electron temperature. The scatter is simulation results using BOUT++, and the red line is linear fitting result.

Furthermore, the nonlinear simulation cases are plotted on the $\ln(Z_{\rm eff}N_{\rm e}R_{\rm imp}) - \ln(T_{\rm e})$ space, and classified by: (I) both bursts, (II) burst A alone, (III) burst B alone and (IV) ELM free (i.e. no burst), as Fig. 7 shows. It can be observed that, four regions are identified according to the difference of the "two-stage burst" feature. The four regions are divided by two intersecting lines. As Fig. 7 shows, the red dashed line represents the onset threshold of burst A, which is the stabilization boundary of peeling-ballooning modes due to impurities, and the black dashed

line represents the onset threshold of burst B, which is the stabilization boundary of drift tearing modes due to impurities.

According to the four parameter regions and features of burst B discussed above, different ELM behaviors to the impurities are listed in Table 1. Here, $I \rightarrow II$ means the operation point shifts from region I to region II due to the impurity seeding.

| TE 11 1 TEL TELLE ' 1 1 ' | 1 / /1 | | | 1.1 | |
|---------------------------------|--------------|------------------|-----------|-----------|-------------|
| Table 1 The ELM size behavior | due to the n | narameter region | Variation | caused by | imniirities |
| Tuble I The ELIVI Size behavior | auc to the p | diameter region | variation | causea oy | mparmes |

| Parameter Region | ELM size | | |
|---|-----------|--|--|
| $I \to I$, $I \to III$, $III \to III$ | No effect | | |
| $I \to II$, $II \to II$ | Mitigate | | |
| $I,II,III \rightarrow IV$ | Suppress | | |

When impurities are seeded into the pedestal, the electron temperature generally decreases and $R_{\rm imp}$ increases, leading the operation point moving towards the "lower temperature and higher impurity effect" direction in the parameter space shown in Fig. 7. Considering $I \rightarrow I$, $I \rightarrow III$ and $III \rightarrow III$ three cases, because the drift tearing mode will eliminate the stabilizing effect of impurities, the impurity dynamics won't contribute to the ELM size reduction, even the peeling-ballooning mode is fully stabilized initially in region III. For $I \rightarrow II$ and $II \rightarrow II$, although the peeling-ballooning mode is not completely stabilized, the stabilization effect of impurities will remain during ELM burst because of the absence of the drift tearing mode. Furthermore, the stabilization effect increases with $R_{\rm imp}$. Therefore, in these cases the ELM size will continuously mitigated with the increase of impurity density. Finally, when the impurity density is high enough to stabilize both peeling-ballooning, a long-lasting ELM free stage will be achieved.

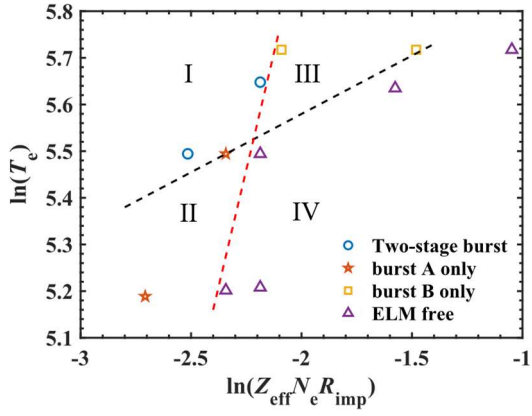


Fig. 7 The R_{imp} – T_e plane is divided in to four regions by the stability boundaries of P-B mode (red dashed curve) and drift-tearing mode (black dashed curve). The feature of ELM dynamic process in the four regions are: I. Two-stage burst (blue circles); II. Burst A only (red stars); III. Burst B only (yellow squares); IV. ELM free (purple triangles).

5. SUMMARY

To investigate the complex impact of impurities on edge localized mode behavior, a systematic simulation study is conducted using the BOUT++ six-field two-fluid model with impurity physics based on an EAST experiment (shot #69033).

Linear simulations reveal that impurities exert an overall stabilizing effect on pedestal in stabilities through additional vorticity introduced by impurities. Theoretical analysis found stabilization effect due to impurity can be characterized by impurity mass density ratio, and shows good agreement with linear simulation results.

However, while the linear growth rate decreases monotonically with increasing impurity density, nonlinear simulations show that the reduction in ELM size exhibits a threshold like response. This complex nonlinear behavior is found to be closely related to the observed "two-stage burst" (burst A and B) phenomenon. While burst A is directly triggered by the linear growth of peeling-ballooning mode, burst B is indirectly triggered by the drift tearing mode. The magnetic flutter raised by drift tearing mode reduces the radial electric field and eliminates the stabilization effect of impurities. Therefore, the overall ELM size remains unaffected unless the burst B is completely suppressed, thus explains the threshold behavior.

Based on this mechanism, the different ELM behavior to the impurity density is explored in $\ln(Z_{\rm eff}N_{\rm e}R_{\rm imp})-\ln(T_{\rm e})$ space. The parameter space is divided into four regions by peeling-ballooning boundary and drift tearing mode boundary, and the different effect of impurity dynamics on the ELM evolution can be explained by the shift of operation point among different regions.

ACKNOWLEDGEMENTS

This work is supported by the National MCF Energy R&D Program of China (Grant No. 2019YFE03030004, 2024YFE03010003, 2019YFE03080500), the National Natural Science Foundation of China (Grant Nos. 11975232). Numerical simulations are carried out using the CFETR Integration Design Platform (CIDP) with the support of the Supercomputing Center of University of Science and Technology of China.

REFERENCES

- [1] A. W. Leonard, Plasma detachment in divertor tokamaks, Plasma Phys. Contr. Fusion 60 (2018) 044001
- [2] G. S. Xu, Y. F. Wang, Q. Q. Yang, et al., Recent advances in developing natural and impurity-induced small/no-ELM H-mode regimes in EAST, Rev. Mod. Phys. 7 (2023) 14
- [3] H. Lan, T. H. Osborne, R. J. Groebner, et al., H-mode pedestal improvements with neon injection in DIII-D, Nucl. Fusion 60 (2020) 056013
- [4] T. H. Osborne, G. L. Jackson, Z. Yan, et al., Enhanced H-mode pedestals with lithium injection in DIII-D, Nucl. Fusion 55 (2015) 063018
- [5] J. Rapp, T. Eich, M. v. Hellermann, et al., ELM mitigation by nitrogen seeding in the JET gas box divertor, Plasma Phys. Contr. Fusion 44 (2002) 639
- [6] X. Lin, G. S. Xu, Q. Q. Yang, et al., Physical mechanisms for the transition from type-III to large ELMs induced by impurity injection on EAST, Phys. Lett. A 431 (2022) 127988
- [7] G. L. Xiao, X. L. Zou, W. L. Zhong, et al., Dual effects of impurity seeding on pedestal turbulence and ELMs in the HL-2A tokamak, Nucl. Fusion 61 (2021) 116011
- [8] T. Y. Xia, X. Q. Xu and P. W. Xi, Six-field two-fluid simulations of peeling-ballooning modes using BOUT++, Nucl. Fusion 53 (2013) 073009
- [9] Z. Li, X. Chen, C. M. Muscatello, et al., Numerical modeling of pedestal stability and broadband turbulence of wide-pedestal QH-mode plasmas on DIII-D, Nucl. Fusion 62 (2022) 076033
- [10] H. Seto, X. Q. Xu, B. D. Dudson, et al., Interplay between fluctuation driven toroidal axisymmetric flows and resistive ballooning mode turbulence, Phys. Plasmas 26 (2019) 052507
- [11] H. Seto, X. Q. Xu, B. D. Dudson, et al., Two-stage crash process in resistive drift ballooning mode driven ELM crash, Phys. Plasmas 31 (2024) 032513
- [12] A. B. Hassam, Fluid theory of tearing instabilities, Phys. Fluids 23 (1980) 2493-2497